Supplementary Figure 1

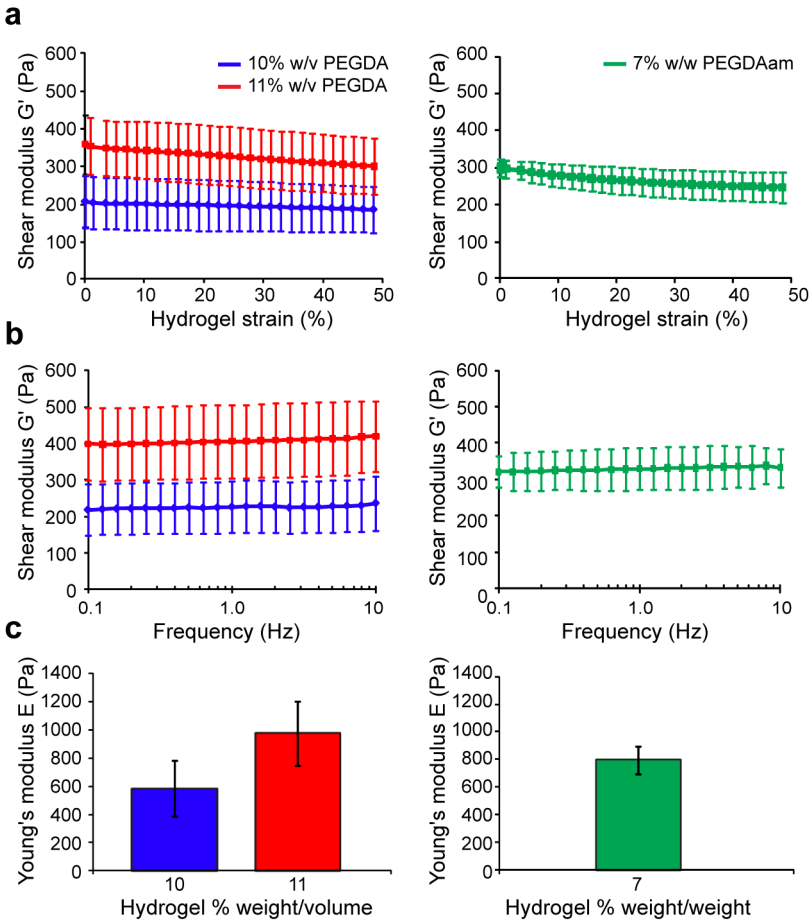

Supplementary Figure 1: Mechanical characterization of hydrogel matrices. Hydrogel mechanics were determined using shear rheology. Swollen, cell-laden hydrogels were measured after three days of culture in growth medium (identical conditions to the measurement of cellular tractions). Samples were compressed to 0.2 N normal force to ensure good contact between the hydrogel and geometry. (**a**) Plot of the shear modulus (G′) as a function of applied radial strain for polyethelyne diacrylate based (PEGDA) and polyethylene diacrylamide-based (PEGDAam) hydrogels. All hydrogels were linear over the ranges of strain measured. Average shear moduli obtained from these plots were 196 ± 66, 328 ± 76 and 267 ± 34 Pa for 10% w/v and 11% w/v PEGDA and 7% w/w PEGDAam hydrogels respectively. (**b**) Plot of the shear modulus (G′) as a function of frequency for PEGDA and PEGDAam hydrogels. Measurements were obtained at 1% radial strain at frequencies varying from 0.1 to 10 Hz. Hydrogel moduli showed no substantial dependence on frequency over the range of applied loadings. (**c**) Young's moduli of PEGDA and PEGDAam hydrogel matrices. Hydrogels were assumed to be nearly incompressible with a Poisson's ratio of 0.49 leading to predicted Young's moduli of 585 ± 196 and 978 ± 228 Pa for 10% w/v and 11% w/v PEGDA and 796 ± 102 Pa for 7% w/w PEGDAam hydrogels respectively. For all plots, errors bars are ± standard deviation from $n = 6$ samples.

Supplementary Figure 2

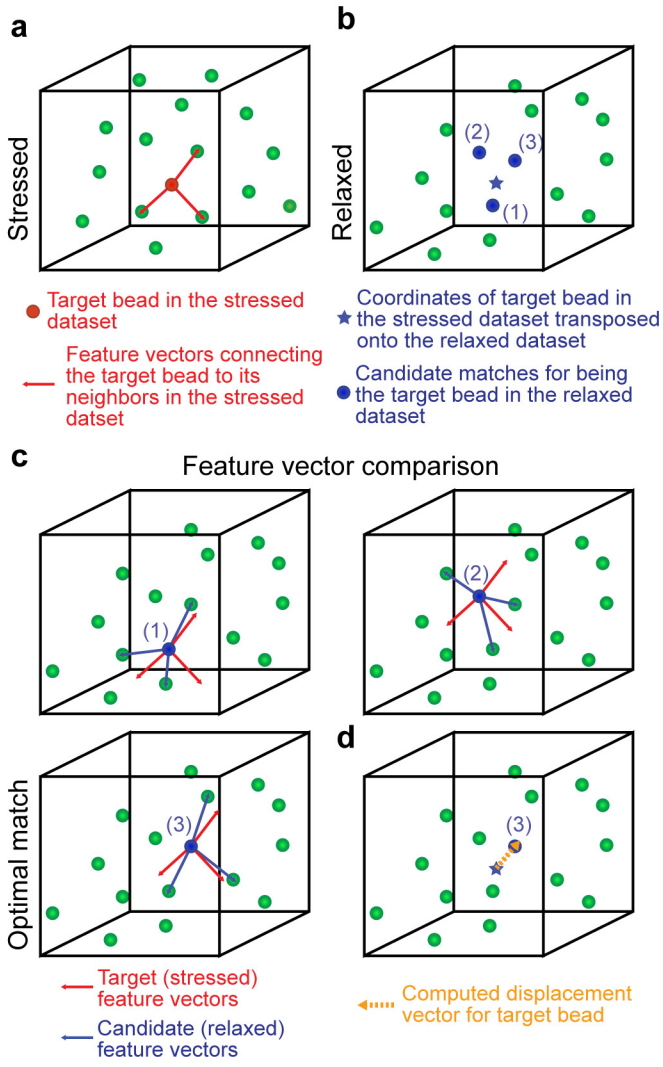

Supplementary Figure 2: Algorithm for tracking bead displacements in 3D. The key challenge to determine the displacement field within the hydrogel is to identify matching beads within the stressed (i.e., subjected to cell generated tractions) and relaxed (after cell lysis) datasets. (**a**) For each bead in the stressed dataset (target beads), feature vectors are drawn to the nearest neighboring beads (target feature vectors). These vectors provide a unique "signature" for each bead. (**b**) The spatial coordinates of a target bead within the stressed dataset are transposed onto the relaxed dataset and neighboring beads within this relaxed dataset are identified as candidate matches. (**c**) For each candidate match in the relaxed dataset, feature vectors are drawn to the nearest neighboring beads. The most closely matching candidate and target feature vectors identify the optimal match (i.e., the same bead has been located in the stressed and relaxed datasets). (**d**) Once a match is made, the displacement is calculated from the spatial coordinates of the matched beads in the stressed and relaxed datasets.

Supplementary Figure 3

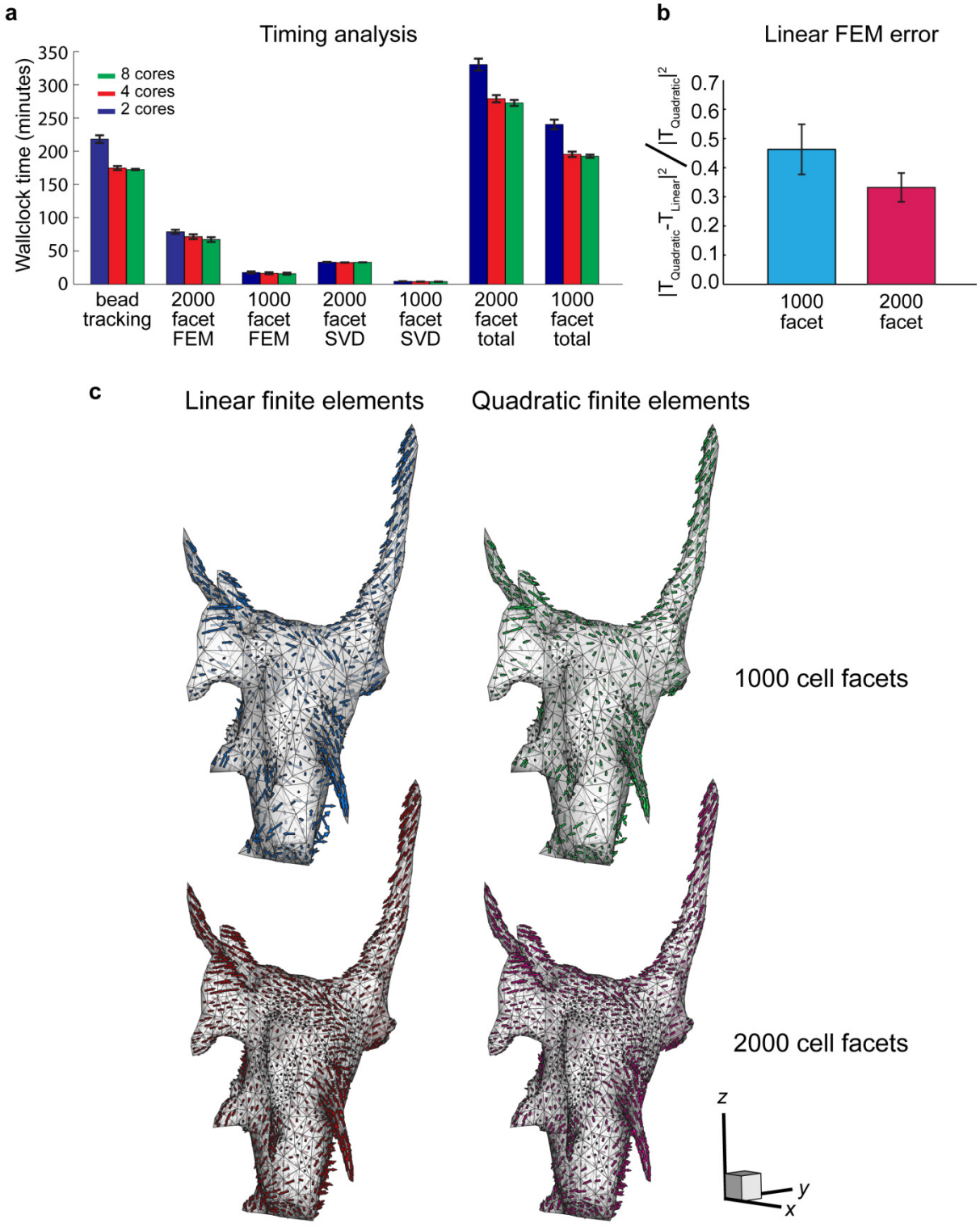

Supplementary Figure 3: Computational requirements and FEM accuracy. (**a**) Plot of the times required for the various steps in the computation of 3D cellular tractions using linear finite elements: bead tracking, finite element computation of the discretized Green's function (FEM), and singular value decomposition (SVD). Data are shown for both simplified (1,000 cellular facets) and complex (2,000 cellular facets) meshes. (**b**) Plot of the error introduced by the complex and simplified meshes used to discretize the cell surface and surrounding hydrogel. The solutions obtained using quadratic elements were used to approximate the exact solution when compared to those obtained with linear elements. (**c**) Vector plots of the tractions computed using the simplified (1,000 cellular facets with linear (blue), or quadratic (green) elements) and complex (2,000 cellular facets with linear (red) or quadratic (magenta) elements) finite element meshes.

Supplementary Figure 4

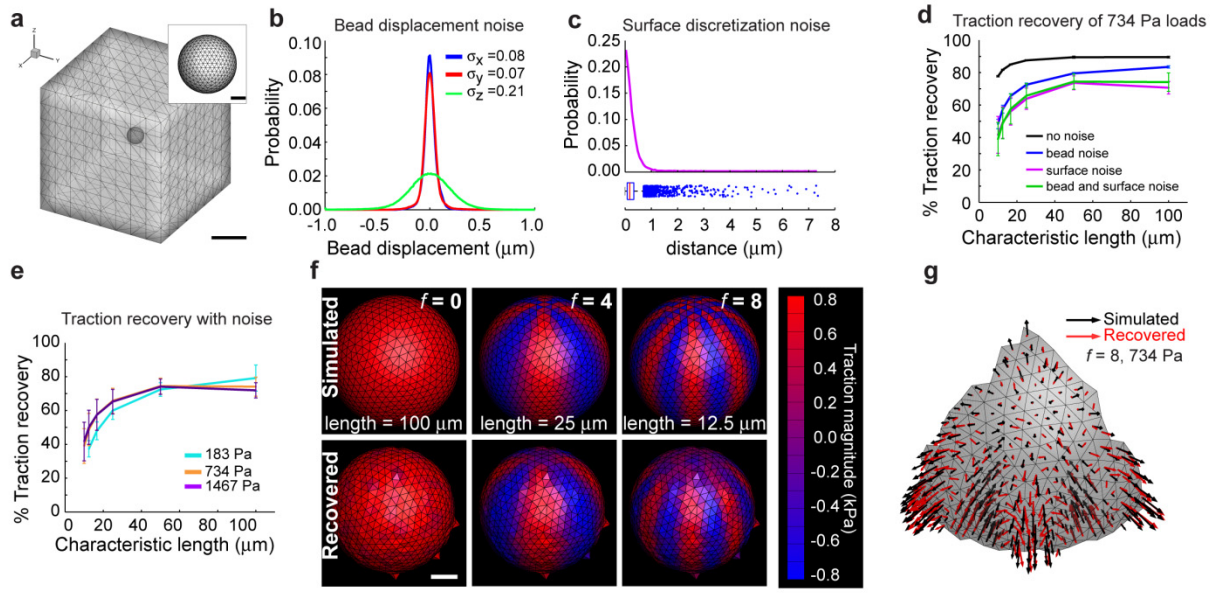

Supplementary Figure 4: Validation using simulated tractions on a spherical cell. (**a**) Computational domain showing surface meshes on the inner cellular sphere (50 μm diameter) and outer cube of matrix (400 μm per side). Scale bar = 100 μm, 10 μm (inset). (**b**) Probability densities of experimentally measured bead displacements (noise) in absence of cells. Measurements are compiled from six separate locations within the gel from several experiments. (**c**) Boxplot and probability density of surface discretization error measured from two independent meshings of seven different cells from multiple experiments. (**d**) Percent of traction recovery summed over all facets, defined as: $\left(1 - \frac{|\mathbf{T}_{\text{recovered}} - \mathbf{T}_{\text{simulated}}|^2}{|\mathbf{T}_{\text{simulated}}|^2}\right)$ x 100, as a function of characteristic length of the simulated loadings (defined as the average period of oscillation on the surface of the sphere). Plotted recoveries are in the presence of no noise, bead noise alone, surface noise alone, and bead and surface noise combined. Error bars are standard deviation on the mean. **e**) Percent of traction recovery as a function of characteristic length in the presence of surface and bead noise for loadings of three different magnitudes that span the range of tractions exerted by cells. Note that the 10 μm, 183 Pa data point is omitted because the L-curve method fails to find an appropriate corner for this loading. **f**) Contour plots showing the magnitude of simulated and recovered tractions on a representative surface in the presence of both bead displacement and surface discretization noise. **g**) Magnified plot of the simulated and recovered tractions on each facet of the cell for one of the most rapidly varying traction fields ($f = 8$, characteristic length = 12.5 μm).

Supplementary Figure 5

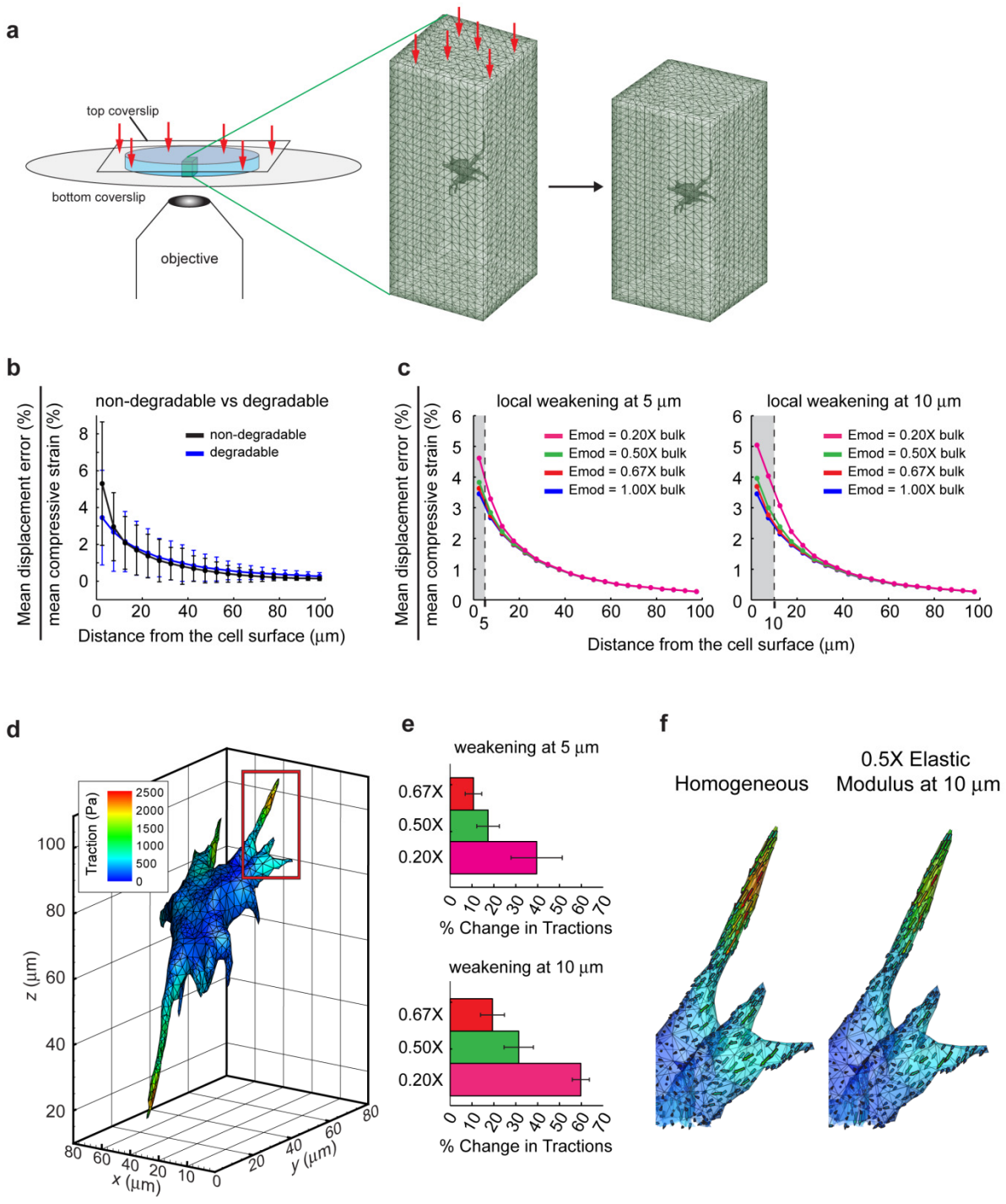

Supplementary Figure 5: Sensitivity analysis of tractions to local hydrogel mechanics. (**a**) Schematic of the experimental setup used to compress hydrogel samples. For a given measurement, the sample was compressed to between 5-7% strain. (**b**) Plot of the errors between the experimental displacements, and those computed using a finite element simulation defined as: $\frac{|\mathbf{d}_{\text{experimental}}-\mathbf{d}_{\text{FEM}}|^2}{|\mathbf{d}_{\text{experimental}}|^2}$, where **d** is the displacement vector relating the positions of a given bead before and after hydrogel compression. Data were binned into 5 μm increments based on the vicinity of a given bead to the cell boundary and the mean value of each bin was used to generate a single curve for each cell. Because the error is expected to scale with strain (given the small strain approximation), these values were normalized by the mean compressive strain for a given sample (which typically varied by ~1-2% between samples). No significant difference was observed between the errors in the degradable and non-degradable hydrogels (P = 0.5 by student t-test on the mean error of the points within 0-20 μm of the void surface). (**c**) Plot of the errors between the experimental and finite element displacements for cells in degradable hydrogels. Finite element models incorporating local heterogeneities were created by setting the modulus of all elements within either 5 or 10 μm of the cell boundary to 0.67X, 0.5X, or 0.2X that of the surrounding material. All heterogeneous models diverged more significantly from the experimental displacements than did the homogeneous model (P = [0.021, 0.020, 0.019] and P = [0.038, 0.016, 0.009] for 0.67X, 0.5X and 0.2X curves at 5 μm and 10 μm respectively by paired student t-test on the mean error of points within 0-20 μm of the void surface). (**d**) Contour plot of the tractions exerted by an NIH 3T3 fibroblast encapsulated in a 978 Pa degradable hydrogel. (**e**) Sensitivity analysis of the computed tractions under heterogeneous mechanical assumptions. Percent change in tractions was calculated as $\frac{|\mathbf{T}_{\text{homogeneous}}-\mathbf{T}_{\text{heterogeneous}}|^2}{|\mathbf{T}_{\text{homogeneous}}|^2}$ x 100 for each of the six heterogeneities tested above. (**f**) Expanded views show the tractions from **d** computed under homogeneous material assumptions, and those computed under the assumption that the Young's modulus of the hydrogel within 10 μm of the cell boundary is 0.5X that of the bulk (i.e. within 10 μm of the cell is 489 Pa). Data from **b**, **c**, and **e** are from n = 3 cells per condition. Error bars in **b** and **e** are ± standard deviation on the mean.

Supplementary Figure 6

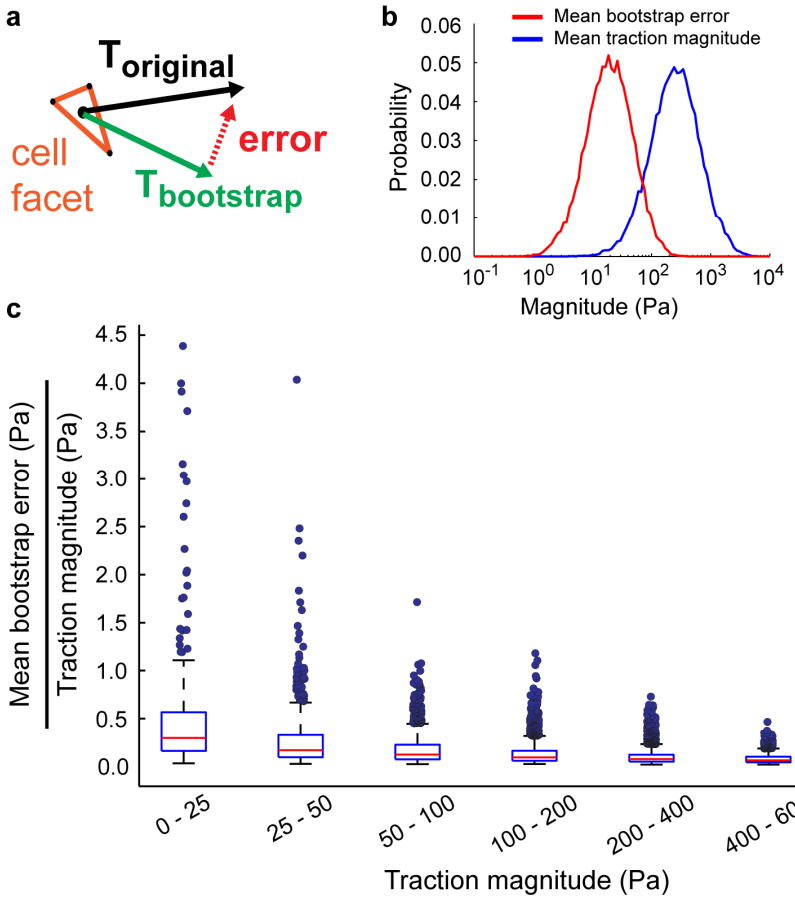

d

Bin Edges (Pa)	Median	25th Percentile	75th Percentile	Number of Observations	Number of Outliers
0 - 25	0.29	0.16	0.57	325	24
25 - 50	0.16	0.09	0.32	1081	51
50 - 100	0.12	0.07	0.22	3091	143
100 - 200	0.09	0.05	0.16	5784	265
200 - 400	0.07	0.04	0.12	6773	332
400 - 600	0.06	0.04	0.09	3076	135
>600	0.04	0.03	0.07	3870	131

Supplementary Figure 6: Bootstrap analysis of tractions. (**a**) Schematic for the computation of bootstrap errors. Experimental noise is superimposed onto best fit displacements (as computed using the L-curve) given by a known traction field ($\mathbf{T}_{original}$) and a new traction field is recovered ($\mathbf{T}_{bootstrap}$). The Euclidian distance between the original and bootstrapped tractions is recorded as the bootstrap error. (**b**) Probability densities of the mean bootstrap error, computed from 100 iterations on the tractions from 12 cells (meshed with 2,000 facets each, yielding 24,000 total measurements of the mean error) and of the original traction magnitudes computed from 12 cells as above. (**c**) Box and whiskers plot of the mean bootstrap error normalized by the original traction magnitude, giving a fold error due to bead displacement uncertainty. (**d**) Table listing the median values, 25th percentile, 75th percentile, number of observations and number of outliers for each bin of **c**.

Supplementary Figure 7

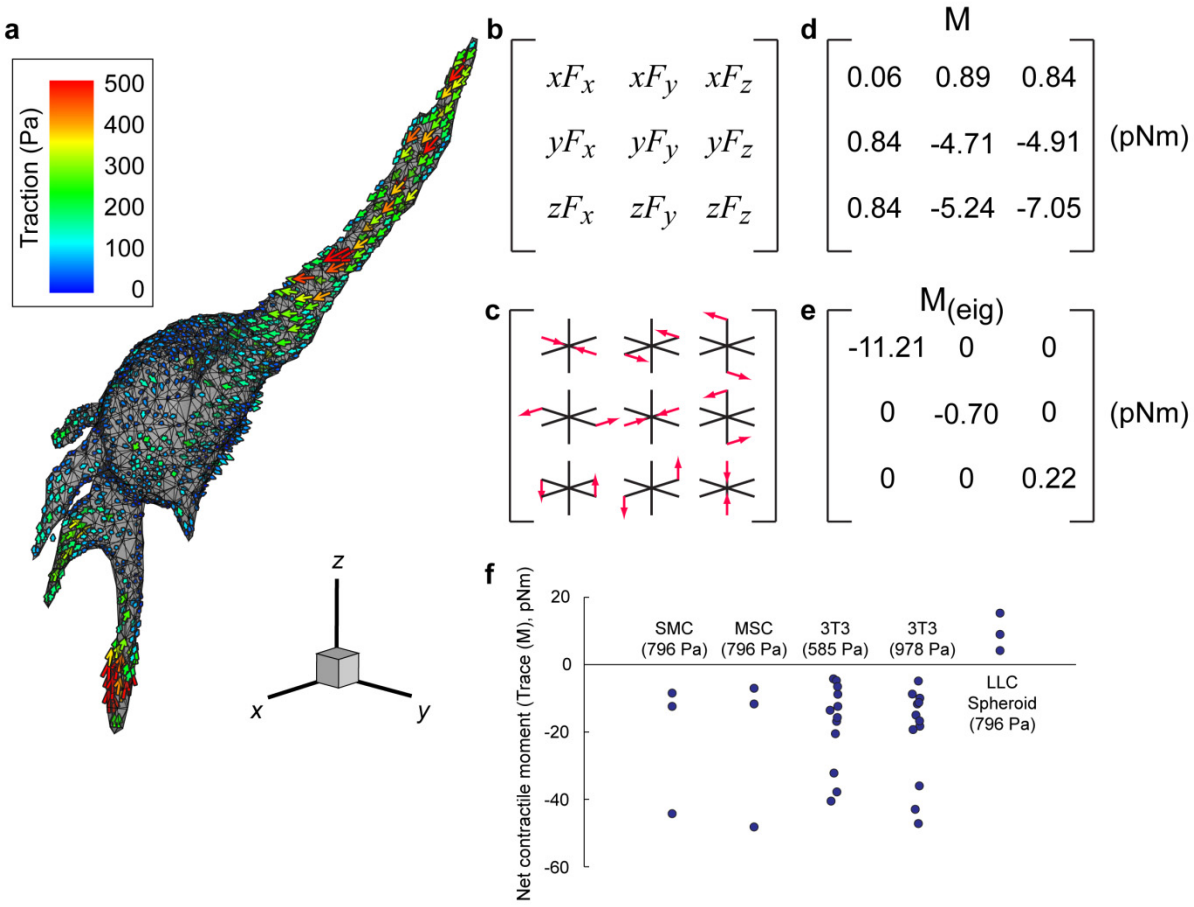

Supplementary Figure 7: Measurement of contractile moments. (**a**) Tractions exerted by a human mesenchymal stem cell encapsulated in a 7% w/w PEGDAam based hydrogel. For clarity, only one half of all vectors are shown. (**b**) Component representation of the contractile moment matrix. The Cartesian coordinates x, y, and z represent the distance of the centroid of a given surface facet from the center of mass of the cell and the forces F_x, F_y, and F_z are the Cartesian components of the force (traction multiplied by facet area) exerted at the corresponding facet. Summation over all facets gives the appropriate term of the moment matrix. (**c**) Schematic of the contractile moment matrix showing the orientation of the terms with respect to the Cartesian axis. (**d**) Contractile moment matrix of the cell in **a**. (**e**) Diagonalized (via eigenvalue decomposition) contractile moment matrix. (**f**) Plot of the net contractile moments of cells and multicellular spheroids.

Supplementary Figure 8

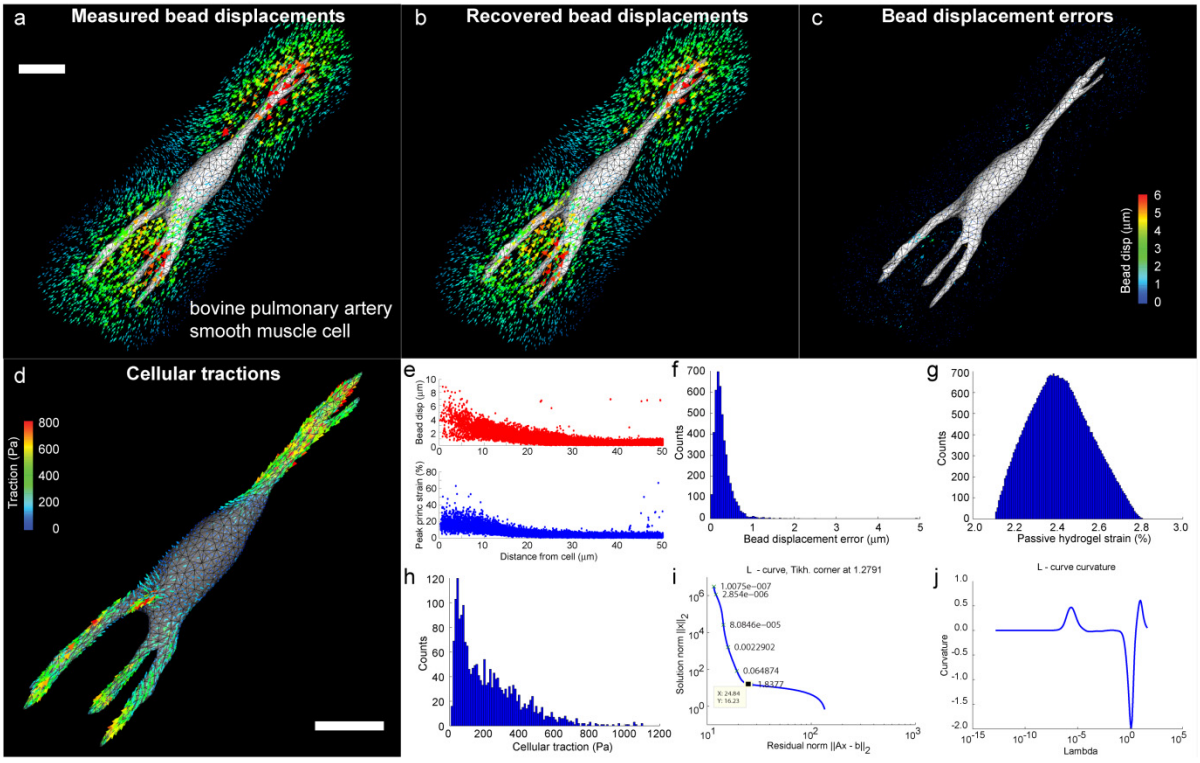

Supplementary Figure 8: 3D traction datasheet. Bovine pulmonary artery smooth muscle cells were encapsulated in a 7% w/w PEGDAam based hydrogel and allowed to spread over 72 hours. To measure the tractions exerted by the cell, volumetric images were acquired before and after treatment with 0.5% SDS. In order to verify the accuracy of the reconstructed tractions, it is useful to generate a datasheet displaying all relevant data for a given cell. (**a**) Surface mesh of the cell showing measured bead displacements in the hydrogel. Scale bar = 20 μm. (**b**) Plot of the "best fit" bead displacements that would be predicted based on the recovered cellular tractions. (**c**) Plot of the errors in bead displacements between the experimentally measured and best fit fields. (**d**) Plot of the tractions exerted by the cell. Scale bar = 20 μm. (**e**) Plots of the bead displacement and peak (maximum magnitude) principal hydrogel strain as a function of distance from the surface of the cell. (**f**) Histogram of the errors between the measured and best fit bead displacements. (**g**) Histogram of the peak principal strains induced by correction for passive hydrogel drift and swelling. (**h**) Histogram of the cellular tractions. (**i**) Plot of the L-curve (log-log plot of the solution norm vs. the residual norm as a function of lambda) used to calculate the correct amount of regularization. The corner of the L-curve indicates the optimal amount of regularization. (**j**) Plot of the curvature of the L-curve showing a distinct minimum in curvature at the optimal value of lambda.

Supplementary Figure 9

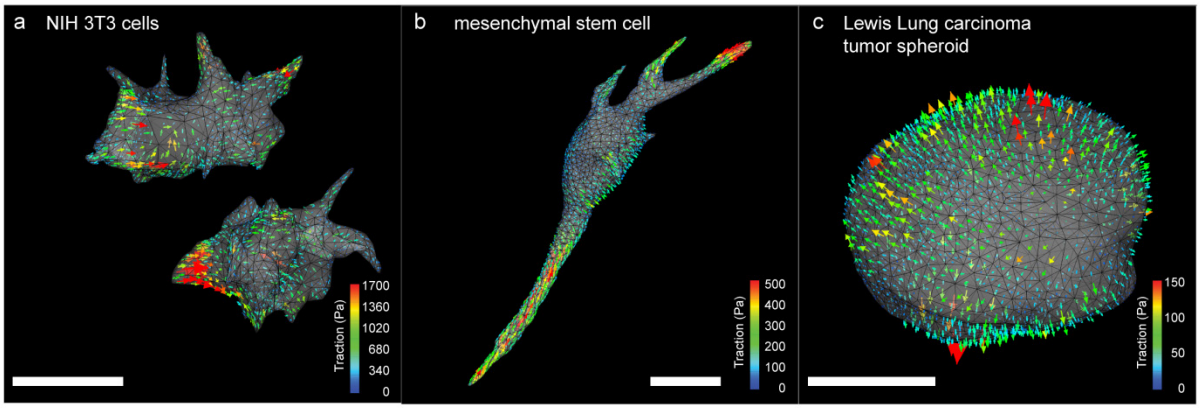

Supplementary Figure 9: Measurement of cellular tractions in different contexts. (**a**) NIH 3T3 fibroblasts were encapsulated in an 11% w/v PEGDA based hydrogel and allowed to spread for 72 hrs. Two cells in the vicinity of each other extend processes preferentially away from the neighboring cell and pull back inward towards their respective centers of mass. These data demonstrate that the more complex configuration of two neighboring cells does not limit the algorithm in its ability to reconstruct tractions. (**b**) Human mesenchymal stem cells were encapsulated in a 7% w/w PEGDAam based hydrogel and allowed to spread over 72 hours. These cells invaded into the surrounding hydrogel with long slender and occasionally branched extensions. Strong forces were located predominantly near the tips of these extensions and pulled inward back toward the center of mass of the cell. (**c**) Lewis lung carcinoma cells were encapsulated in a 7% w/w PEGDAam based hydrogel and cultured for 72 hrs. During this time, the cells did not invade into the surrounding hydrogel as did the other cell types measured, but rather rapidly proliferated forming a multicellular spheroid. The expanding spheroid deformed the surrounding hydrogel and exerted predominantly outward normally directed tractions that were distributed over the surface of the multicellular structure. Such 'pressures' have been observed in large tumor masses, but not previously appreciated in small spheroids. All scale bars = 20 μm.

Supplementary Figure 10

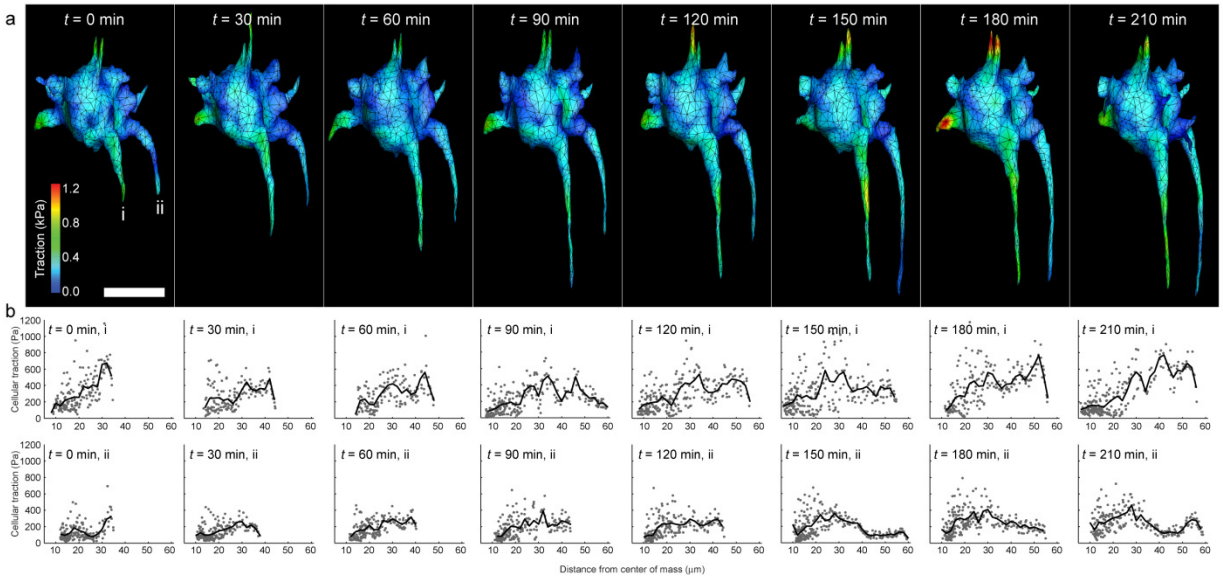

Supplementary Figure 10: Measurement of dynamic tractions exerted by spreading cells. NIH 3T3 fibroblasts were encapsulated in an 11% w/v PEGDA based hydrogel and allowed to begin spreading. The cell and surrounding hydrogel were then imaged for 3.5 hours in 30 minute intervals. (**a**) During this time, the labeled extensions (i and ii) exerted tractions as they extended into the matrix. Interestingly, this spreading seemed to be biased, occurring only on one face of the cell. In contrast, strong forces were also exerted by small dynamic protrusions on the face of the cell opposite these spreading extensions. Scale bar = 20 μm. (**b**) Tractions exerted by the extensions labeled in **a** are plotted as a function of the distance from the center of mass of the cell. Consistent with our observations from other cells, these invading structures showed strong forces proximal to the leading edge, with a drop in traction near the tip.

SUPPLEMENTARY NOTE 1

Calculation of bead displacements and hydrogel strain

Multipage TIFF images of the hydrogel exterior to the cell were imported into Matlab (The Mathworks) and bead centroids were identified as described previously[1]. Once bead centroids were identified, beads in the stressed (subject to cell generated tractions) dataset were matched to beads in the relaxed (after cell lysis) dataset using a feature vector-based algorithm relating the relative position of each bead to its local neighbors (**Supplementary Fig. 2**). For each target bead to be matched in the stressed dataset, feature vectors were generated to its nearest neighbors, measured by the Euclidian distance between bead centroids (**Supplementary Fig. 2a**). Candidate matches for the target bead in the relaxed dataset were identified as those beads nearest to the spatial coordinates of the target bead in the stressed dataset (**Supplementary Fig. 2b**). For each of these candidate matches, feature vectors were generated to the nearest neighbors in the relaxed dataset and compared to the target feature vectors (**Supplementary Fig. 2c**). The candidate bead with feature vectors most closely matching the target bead was identified as being the same bead in the stressed and relaxed datasets, and the displacement recorded (**Supplementary Fig. 2d**). The number of target feature vectors, candidate matches, and candidate feature vectors can be optimized for a given displacement field; however, it is in general necessary to include a greater number of candidate feature vectors than target feature vectors as the relationship between nearest neighbors can change between the stressed and relaxed datasets. In these cases, the best matching candidate feature vectors are used.

To compute the bead displacements used for calculating cellular tractions, we implemented two rounds of bead tracking as follows. A preliminary round of bead tracking was performed to identify initial bead displacements. To correct for temperature-dependent swelling and mechanical drift in the gel, we applied a quadratic correction to the displacement of all beads, computed by minimizing the total bead displacement as follows. We defined the objective function as:

$$\min\left|\mathbf{C}_{\text{stressed}} - \mathcal{F}\{\mathbf{C}_{\text{relaxed}}\}^{\mathrm{T}}\right|^2 \quad (1)$$

Unless otherwise designated, all norm symbols signify the Frobenious norm. $\mathbf{C}_{\text{stressed}}$ and $\mathbf{C}_{\text{relaxed}}$ are m x 3 matrices in which each row is the position vector of a bead centroid in the stressed or relaxed dataset and m is the total number of beads tracked. The function $\mathcal{F}$ accepts the centroids of the beads in the relaxed dataset and shifts the x, y, and z components according to a quadratic correction.

$$\mathcal{F}_{ij}\{\mathbf{C}\} = \sum_{k=1}^{3}\left(Q_{jk}(C_{ik})^2 + A_{jk}C_{ik} + d_j + M_{jk}C_{ik}\sum_{l=1}^{3} C_{il}P_{kl}\right) \quad (2)$$

where Q and M are matrices containing coefficients of quadratic terms of single and mixed variables respectively, A and d contain affine terms, $(C_{ik})^2$ represents the square of component *ik* of C, and P is the following permutation matrix: [0,1,0;0,0,1;1,0,0]. Together, Q, M, A, and d comprise 30 terms over which the optimization of equation (2) was carried out using built-in functions for constrained non-linear optimization in Matlab. After applying this correction, a second round of bead tracking was performed to compute the final displacement field, which was then processed using a running average filter to remove misidentified beads.

To compute the strain in the hydrogel surrounding the cells, bead displacements were interpolated onto a uniform 4 μm cubic grid using Matlab. This grid size was chosen to be just greater than the average distance between beads. The Green-St. Venant (Lagrangian) strain tensor, $\mathbf{E}=(\mathbf{F}^{\mathrm{T}}\mathbf{F}-\mathbf{1})/2$, was estimated at the center of each element, where **1** is the identity tensor and the deformation gradient **F** was estimated using standard tri-linear interpolation shape functions.

REFERENCES FOR SUPPLEMENTARY NOTE 1

1. Gao, Y.X. & Kilfoil, M.L. Accurate detection and complete tracking of large populations of features in three dimensions. *Opt Express* **17**, 4685-4704 (2009).

SUPPLEMENTARY NOTE 2

Generation of a discretized Green's function and calculation of cellular tractions

We generated a discretized Green's function relating tractions on the cell surface to displacements within the gel using the finite element method. 3D tetrahedral meshes were obtained as described in **Methods**, and used to generate the forward solution relating bead displacements in the gel to unit tractions applied to each facet on the surface of the cell in each of the three Cartesian directions. From each of these solutions, the experimentally measured bead coordinates were queried for the computed displacements. Because both the bead coordinates and the location of applied tractions are at discrete locations, the relation between bead displacements within the gel $\mathbf{u}$ and tractions on the surface of the cell $\mathbf{T}$ is now transformed into a set of linear equations

$$\mathbf{u} = \Gamma\mathbf{T} \quad (1)$$

where we have adopted the notation used in ref [1] in which

$$\mathbf{u} = [u_1^1(\mathbf{r}); u_2^1(\mathbf{r}); u_3^1(\mathbf{r}); u_1^2(\mathbf{r}); u_2^2(\mathbf{r}); u_3^2(\mathbf{r}); \ldots; u_1^m(\mathbf{r}); u_2^m(\mathbf{r}); u_3^m(\mathbf{r})]$$

is a 3m column vector, where m is the number of tracked beads and $\mathbf{r}$ is the position vector of each bead.

$$\mathbf{T} = [T_1^1(\mathbf{r}'); T_2^1(\mathbf{r}'); T_3^1(\mathbf{r}'); T_1^2(\mathbf{r}'); T_2^2(\mathbf{r}'); T_3^2(\mathbf{r}'); \ldots; T_1^n(\mathbf{r}'); T_2^n(\mathbf{r}'); T_3^n(\mathbf{r}')]$$

is a 3n column vector, where n is the number of discretized facets on the surface of the cell and $\mathbf{r}'$ is the position vector of each facet. Subscripts for both *u* and *T* in these definitions represent displacements and tractions respectively along each Cartesian axis.

$\boldsymbol{\Gamma}$ is an m x n matrix of the following form:

$$\Gamma_{ij}^{mn} = \begin{bmatrix} G_{ij}^{11} & \cdots & G_{ij}^{1n} \\ \vdots & \ddots & \vdots \\ G_{ij}^{m1} & \cdots & G_{ij}^{mn} \end{bmatrix} \quad (2)$$

Each element of $\boldsymbol{\Gamma}$ is a 3 x 3 submatrix relating the displacement of bead m in direction i in response to a load on facet n in direction j:

$$G_{ij} = \begin{bmatrix} g_{11} & g_{12} & g_{13} \\ g_{21} & g_{22} & g_{23} \\ g_{31} & g_{32} & g_{33} \end{bmatrix} \quad (3)$$

We used 0[th] order Tikhonov regularization together with the L-curve criterion[2] for implementing and choosing the correct value for the Lagrange parameter, λ, resulting in the following optimization:

$$\min\{|\boldsymbol{\Gamma}\mathbf{T} - \mathbf{u}|^2 + \lambda^2|\mathbf{T}|^2\} \quad (4)$$

This optimization problem was solved by singular value decomposition using the suite of Matlab routines "*Regularization tools*" by PC Hansen[3]. To save computational resources, only the displacements of beads within 20 μm from the cell surface were used to calculate cellular tractions. Incorporating measurements of beads greater than 20 μm from the cell surface did not substantially change the recovered tractions.

REFERENCES FOR SUPPLEMENTARY NOTE 2

1. Schwarz, U.S. et al. Calculation of forces at focal adhesions from elastic substrate data: the effect of localized force and the need for regularization. *Biophys J* **83**, 1380-1394 (2002).
2. Hansen, P.C. in Computational Inverse Problems in electrocardiography (Advances in Computational Bioengineering), Vol. 5. (ed. P.R. Johnston) 119-142 (WIT Press, Southampton; 2001).
3. Hansen, P.C. Regularization Tools Version 4.0 for Matlab 7.3. *Numerical Algorithms* **46**, 189-194 (2007).

SUPPLEMENTARY NOTE 3

Computational resources and finite element accuracy

To illustrate the computational requirements necessary for the calculation of cellular tractions, we performed timing analysis of the various steps. The main computational steps in our analysis are 1) bead tracking, 2) finite element computation of a numerically generated Green's function, and 3) singular value decomposition of the discretized Green's matrix. The computational expense of each of these steps depends on the complexity and resolution of the finite element mesh used to discretize the cell and surrounding hydrogel, and the number of beads tracked in each measurement. As stated in **Methods**, all data presented in the manuscript were calculated using a Dell Precision T7400 workstation equipped with dual quad core Intel Xeon processors and 16 GB of RAM. Because many of the algorithms in each step can take advantage of parallel processing, we compared the time required using two, four and eight CPU's (**Supplementary Fig. 3a**). The total time required to calculate cellular tractions was approximately 4.5 hours per dataset with the majority of this time spent on computing the bead displacements. Additionally, we report the time required to compute tractions on a simplified finite element mesh. These simplified meshes dramatically reduce the computational requirements and time (down to 3.3 hrs per dataset), yet still capture the fundamental aspects of the cellular tractions. To determine the error introduced by using these finite element meshes, we compared the computed tractions obtained with linear elements versus quadratic elements. The tractions computed using 2,000 linear elements to discretize the cell surface differed by approximately 30% from those using quadratic elements while tractions computed using a simplified mesh of 1,000 linear elements differed by approximately 45% (**Supplementary Fig. 3b**). Nonetheless, in each of these cases, the qualitative differences between the tractions computed using linear or quadratic elements were nearly indistinguishable (**Supplementary Fig. 3c**). It should be noted, however, that coarser discretizations of the cell surface may introduce additional error due to the inability of highly simplified meshes to accurately capture complex cellular morphologies.

Validation using simulated tractions

In order to validate the method and assess the resolution of traction reconstructions, we used simulated loadings on a simplified spherical cell (**Supplementary Fig. 4a**). Oscillating tractions were modeled with amplitudes that varied sinusoidally with respect to the spherical coordinate θ, and three different loadings were chosen to cover the range of tractions exerted by cells (± 183, ± 743 and ± 1467 Pa)**.** The frequency (*f*) was varied from two to ten periods per 360 degrees. Bead displacements were then solved using the forward finite element solution. Experimentally measured noise was then superimposed onto these displacements and the corresponding loadings were recovered (see **Methods** for more detail). In this setting, there are two primary sources of experimental noise: 1) uncertainty of the bead displacements, and 2) uncertainty in the discretization of the cell surface. Our bead tracking resolution was approximately ± 0.075 μm and ± 0.210 μm (standard deviation) in the horizontal and axial planes respectively (**Supplementary Fig. 4b**), whereas the uncertainty of the discretized cell surface was non-normally distributed with a median magnitude of 0.176 μm (**Supplementary Fig. 4c**). In absence of noise, the accuracy of the recovered tractions decreased with the characteristic length of the simulated loadings, but generally matched to within 20% for all original loadings measured. Addition of bead displacement error or surface discretization error, either alone or in combination, reduced accuracy of the recovered loadings by an additional 10-30% (**Supplementary Fig. 4d**). The reconstruction was also sensitive to the magnitude of the applied loadings, since these determined the magnitude of the bead displacements and consequently the signal to noise ratio for any given measurement. Oscillating loadings with amplitudes of either ± 1467 or ± 734 Pa showed little difference in the accuracy of the recovered tractions. However, loadings with an amplitude of ± 183 Pa were more sensitive to experimental noise, with the L-curve method failing for loadings with a characteristic length of 10 μm (**Supplementary Fig. 4e**). However, despite these limitations, the general periodic features of even the more complex simulated loadings were still captured (**Supplementary Fig 4f, g**).

Assessment of local hydrogel mechanics and sensitivity analysis of the recovered tractions

Because cell spreading and invasion require the use of degradable hydrogels, it is possible that the local mechanics near the cell membrane may weaken relative to the bulk hydrogel properties. To test this possibility, we measured the hydrogel deformation near and far from the voids where cells were previously located (i.e. after treatment with SDS) in response to a well defined compressive load in both degradable and non-degradable PEG gels (**Supplementary Fig. 5a**). We compared displacement fields obtained experimentally versus those generated by finite element simulations using homogeneous material properties (reported as error in **Supplementary Fig. 5b**), and found no significant difference between the degradable and non-degradable materials, suggesting that local degradation exterior to the cell is not occurring in the degradable gels or not to an extent that contributes to alterations in bead displacements. Further supporting this conclusion, finite element simulations that incorporate local weakening of the hydrogel near the cell boundary diverge to a greater extent from the observed experimental displacements than do those using a homogeneous material assumption (**Supplementary Fig. 5c**). Importantly, because our method calculates a numerical Green's function, we are able to use all bead measurements with suitable signal to noise (often up to 20 μm or greater from the cell surface), and as a result, traction recovery is relatively insensitive to small local changes in material properties. This can be illustrated by setting all finite elements near the cell surface to be locally weaker than the surrounding hydrogel and then computing the tractions based on experimentally observed bead displacements. For example, a 50% decrease in local modulus within 5 μm of the cell changed the calculated tractions in by approximately 15% when compared to homogeneous conditions, whereas a 50% decrease in local modulus within 10 μm of the cell changed the tractions by approximately 30% (**Supplementary Fig. 5d, e**). Even under these conditions (i.e. a 50% decrease at 10 μm from the cell), the computed tractions were still qualitatively similar to those under the homogeneous assumption (**Supplementary Fig. 5f**).

Bootstrap analysis

Bootstrap analysis is a useful method to determine the effects of bead displacement uncertainty on the traction measurements for actual cells[1, 2]. Briefly, after computation of the tractions for a given cellular geometry, the forward solution is solved to record the best fit bead displacements (i.e. the bead displacements that would be predicted from the computed tractions). Experimental noise, measured as described in **Methods**, was then randomly sampled and superimposed onto these displacements and the inverse problem was solved to recover a new traction field. The difference between the original tractions and the recovered bootstrap tractions gives a measurement of the possible variation in tractions that could be attributed to noise (**Supplementary Fig. 6a**). We computed the mean bootstrap error for each traction measurement from 100 bootstrap iterations (ie 100 independent, random samples of experimental noise) and compiled measurements of the mean bootstrap error from traction measurements of 12 total cells (encapsulated in 978 Pa hydrogels and meshed with 2,000 facets each to yield 24,000 traction measurements). Bootstrap errors were predominantly in the range of 25-75 Pa, which gives a lower bound on the sensitivity of the traction measurements. In contrast, traction magnitudes were substantially higher (**Supplementary Fig. 6b**). Box and whiskers plots of the relative magnitude of bootstrap error compared to the traction magnitudes reveal that bead displacement uncertainty contributes roughly 10 percent uncertainty to the reported tractions (based on median values) (**Supplementary Fig. 6c, d**). This contribution is higher for smaller tractions (e.g. below 50 Pa), but substantially reduced for larger tractions.

Measurement of contractile moments

A useful metric for quantifying cellular tractions is the "contractile moment"[3], defined here as $M_{ij} = \int r_i F_j(\mathbf{r}) d\mathbf{r}$ where r_i are the Cartesian components of the position vector for a given cell facet with respect to the center of mass of the cell, and F_j are the Cartesian components of the force (traction multiplied by facet area) exerted at the corresponding facet (**Supplementary Fig. 7a-d**). The diagonal terms of this

matrix are associated with dilatational or contractile tractions, while the off diagonal terms are associated with tractions that exert torques about the center of mass of the cell. The near symmetric nature of these matrices (before any correction) is indicative of torque equilibrium. After symmetrization (by taking the mean of the off-diagonal terms), the contractile moment matrix can be diagonalized by eigenvalue decomposition ($\mathbf{M}_{eig}$) to reveal the principal contractile (or dilatational) terms (**Supplementary Fig. 7e**). We found that the contractile moments of the cells in this study were of similar order to those presented in ref [3] for cells cultured on top of a planar fibronectin coated polyacrylamide gel with Young's modulus of ~1,200 Pa, which suggests that a change in dimensionality alone (i.e. cells fully encapsulated within a 3D matrix as opposed cultured on top of a 2D planar surface) does not dramatically alter the total contractile potential of a cell. This is further quantified by the trace of the contractile moment matrix which gives the net contractile moment of the cell. This scalar invariant can be used as a metric for total cellular contractility. All single cells measured demonstrated a negative net moment (indicating net inward contraction), whereas the multicellular tumor spheroids demonstrated a positive net moment (indicating expansion or dilation) (**Supplementary Fig. 7f**).

REFERENCES FOR SUPPLEMENTARY NOTE 3

1. Dembo, M. & Wang, Y.L. Stresses at the cell-to-substrate interface during locomotion of fibroblasts. *Biophys J* **76**, 2307-2316 (1999).
2. Schwarz, U.S. et al. Calculation of forces at focal adhesions from elastic substrate data: the effect of localized force and the need for regularization. *Biophys J* **83**, 1380-1394 (2002).
3. Butler, J.P., Tolic-Norrelykke, I.M., Fabry, B. & Fredberg, J.J. Traction fields, moments, and strain energy that cells exert on their surroundings. *Am J Physiol Cell Physiol* **282**, C595-605 (2002).